Title

Molecular Dynamics Simulations of the Eye Lens Water Channel Aquaporin 0 from Fish.

Authors

Freites, Juan

Tobias, Douglas

Publication Date

2024-07-25

DOI

10.1021/acs.jpcb.4c03015

Peer reviewed

THE JOURNAL OF PHYSICAL CHEMISTRY B
A JOURNAL OF THE AMERICAN CHEMICAL SOCIETY

pubs.acs.org/JPCB
Article

Molecular Dynamics Simulations of the Eye Lens Water Channel Aquaporin 0 from Fish

Published as part of The Journal of Physical Chemistry B virtual special issue "Membrane Protein Simulations".

J. Alfredo Freites and Douglas J. Tobias*

Cite This: *J. Phys. Chem. B* 2024, 128, 7577−7585
Read Online
ACCESS | Metrics & More | Article Recommendations

ABSTRACT: Aquaporin 0 (AQP0) plays a key role in water circulation in the eye lens through a variety of functions. In contrast to mammalian genomes, zebrafish contains two *aqp0* genes leading to a separation of AQP0 multiple functions between the two gene products, Aqp0a and Aqp0b. A notable feature of the zebrafish AQP0 paralogs is the increased water permeability of Aqp0b relative to Aqp0a as well as a severa lfold increase relative to mammalian AQP0. Here, we report equilibrium molecular dynamics (MD) simulations on the microsecond timescale to identify the structural basis underlying the differences in water permeability between zebrafish AQP0 paralogs and between AQP0 mammalian and fish orthologs. Our simulations are able to reproduce the experimental trends in water permeability. Our results suggest that a substitution of a key Y23 residue in mammalian AQP0 for F23 in fish AQP0 orthologs introduces significant changes in the conformational dynamics of the CS-I structural motif, which, in conjunction with different levels of hydration of the channel vestibule, can account for the differences in permeabilities between fish and mammalian AQP0 orthologs and between zebrafish AQP0 paralogs.

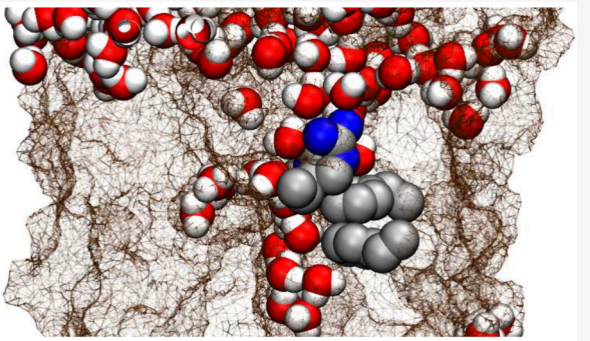

INTRODUCTION

The vertebrate eye lens is a highly conserved organ that focuses light on the retina by the transmission and refraction of light through transparent tissue.[1] Because of the transparency requirement, the eye lens is avascular and relies on a specialized microcirculatory system for homeostasis.[1] Aquaporin 0 (AQP0) is almost exclusively expressed in the eye lens where it plays a critical, but not fully understood, role in the establishing and maintenance of this microcirculatory system.[2] AQP0 has been shown to have multiple functions in the eye lens as a water channel,[3−6] a cell adhesion molecule,[7−11] and a structural protein.[12−14] Loss of AQP0 function disrupts lens development and causes cataracts.[5,11,15−17]

Aquaporins (AQPs) are a ubiquitous family of integral membrane proteins, present in all kingdoms of life, that selectively transport water across membranes.[18,19] AQPs assemble as tetramers. Each protein subunit folds as a six-helix bundle with an hourglass architecture that forms a single-file water conduction pathway ending in a vestibule on either side.[19] Two highly conserved Asn-Pro-Ala (NPA) structural motifs located at the center of the channel form a proton-exclusion site.[19,20] In the extracellular vestibule, a narrow constriction site, termed ar/R or CS-I, formed by conserved Arg, His, and Phe side-chains (R187, H172, and F48 in AQP0) provides a steric barrier to larger molecules as well as an exclusion site for metal ions.[19,21] In the case of mammalian AQP0, structural studies and simulations (reviewed in ref 22) have revealed two additional structural features in addition to CS-I that modulate water permeability: an additional constriction site (CS-II) at end of the single-file pathway on the intracellular side, formed by the side-chains of Y149, F75, and H66, that appears to be gated by Y149, and the Y23 side-chain located between CS-I and the center of the water permeation pathway, whose hydroxyl group may participate in the single-file configuration.[8,9]

Zebrafish has emerged as a suitable model organism to study AQP0 *in vivo*.[5,6,11,23,24] Due to an ancient whole genome duplication event, zebrafish has produced two orthologs of the *aqp0* gene.[25] The duplicated *gene products*, Aqp0a and Aqp0b, have evolved distinct functions in eye lens, both of which are performed by mammalian AQP0.[6,11,24] This separation of the

Received: May 7, 2024
Revised: July 2, 2024
Accepted: July 9, 2024
Published: July 25, 2024

functions of Aqp0a and Aqp0b can be used to dissect the multiple functions of single mammalian AQP0.

Despite sharing ∼70% sequence identity and ∼90% sequence similarity, the water permeability of zebrafish Aqp0a and Aqp0b are severalfold larger than mammalian AQP0[23,26] and similar to that of the AQP0 homolog from killifish.[23] Furthermore, the water permeability of Aqp0b is larger than Aqp0a by a factor 1.5−2 depending on pH.[26] A key difference between the mammalian and fish sequences is the substitution of the key Tyr residue at position 23 for a Phe residue. The behavior of the mammalian AQP0 Y23F mutant has been used to account for the differences in permeability between mammalian and killifish AQP0.[27] However, the Y23F substitution alone cannot explain the differences in permeability of killifish AQP0 and zebrafish Aqp0a with zebrafish Aqp0b. Similarly, a zebrafish Aqp0b variant with a G19S substitution exhibits negligible water permeation in oocyte swelling assays.[23]

To begin to understand the basis for the differences in water permeability between zebrafish Aqp0a and Aqp0b and between AQP0 mammalian and fish orthologs, we performed equilibrium MD simulations on the microsecond timescale. Our simulations allow for the adequate sampling of water permeation in the absence of an osmotic gradient, leading to relative diffusional permeability coefficient estimates that are consistent with experimental permeability measurements under an osmotic gradient. A detailed characterization of the dynamics of single-file water chains and their interactions with key structural features in the AQP0 pathway allows us to identify key differences between most likely states of the channel between the different AQP0s. Our results suggest that the F23 substitution in fish AQP0 orthologs goes beyond the simple removal of the Y23 *phenolic* barrier found in mammalian AQP0. The Tyr to Phe substitution also introduces significant changes in the conformational dynamics of the CS-I structural motif, which together with variations in the hydration of the channel extracellular vestibule can account for the differences in permeabilities between fish and mammalian AQP0 orthologs and between zebrafish AQP0 orthologs.

METHODS

Simulation Systems. Each simulation system consisted of a single aquaporin tetramer embedded in a mixed palmitoyloleoylphosphatidylcholine (POPC), palmitoylsphingomyelin (PSM), and cholesterol bilayer (POPC:PSM:cholesterol, 0.45:0.35:0.20 molar fractions; 563 lipids) in excess 150 mM NaCl (≈60 waters/lipid). The total number of atoms was 183,028 for bovine AQP0 (BtAQP0), 186,798 for killifish AQP0 (FhAqp0), 186,264 for zebrafish Aqp0a (DrAqp0a), and 187,811 for zebrafish Aqp0b (DrAqp0b). The crystallographic structure of bovine aquaporin 0[21] (PDB ID 1ygm) was used as the initial configuration for the BtAQP0 system. The AlphaFold structure predictions[28] from the AlphaFold Protein Structure Database[29] were used as initial configurations for all the fish AQP0 simulation systems (FhAqp0: AFDB ID AF-Q9PUE2-F1; DrAqp0a: AFDB ID AF-Q6DEI6-F1; DrAqp0b:FDB AF-Q4ZJI3-F1). All structure predictions were reported as last updated in AlphaFold DB version 2022-11-01 and created with the AlphaFold Monomer v2.0 pipeline. The pairwise C_α root mean-squared deviations between the AlphaFold models over the entire transmembrane region of the protein chain (residues 7 through 221) are in the range 0.4−0.6 Å, and those between models and the bovine AQP0 crystallographic structure are in the range 1.2−1.3 Å. The full simulation system initial configurations were generated using Membrane Building in CHARMM-GUI[30,31] and the VMD 1.9.4 software package[32] with the positioning of the protein along the transmembrane direction as predicted by the PPM server.[33]

MD Simulations. The simulations were performed using the NAMD software package.[34] Each simulation system was subjected to 1000 steps of conjugate gradient energy minimization, followed by a 200 ps run at constant temperature (310 K) and constant volume with harmonic restraints on the protein heavy atoms. The harmonic restraints were progressively released over five 200 ps runs at constant temperature (310 K) and pressure (1 atm). Production runs were conducted at constant temperature (310 K) and pressure (1 atm). Pre-equilibration runs were performed with NAMD2.14. Production runs were performed with NAMD3a9. The CHARMM36m[35] and CHARMM36[36] force fields were used to model the protein and lipids, respectively. The TIP3P model was used for water.[37] The smooth particle-mesh Ewald summation method[38,39] was employed for the calculation of electrostatic interactions. Short-range real-space interactions were cut off at 12 Å by employing a force-based switching function. A reversible timestep algorithm[40] was used to integrate the equations of motion with a timestep of 4 fs for electrostatic forces and 2 fs for short-range nonbonded forces and bonded forces. All bond lengths involving hydrogen atoms were held fixed using the SHAKE algorithm.[41] A Langevin dynamics scheme was used for temperature control, and a Nosé−Hoover−Langevin piston was used for pressure control.[42,43] Trajectory analyses and visualizations were performed with VMD 1.9.4[32] and R.[44]

Permeability Computations. We tracked the position of each water oxygen along the transmembrane direction over the entire simulation trajectory and recorded a permeation event every time a water molecule crossed both membrane surface planes sequentially. Membrane surface planes, roughly dividing the POPC headgroups and the bulk solvent, were defined as those located 8 Å away from the instantaneous mean position of the POPC carbonyl carbons in each lipid bilayer leaflet and toward the solvent. The specific 8 Å value was determined from the water density profile as the minimum position along the transmembrane direction (from the carbonyl carbon mean position) at which the water density reaches bulk value. Each permeation event was time recorded after the second plane crossing was detected. Events in each flow direction (from the extracellular side to the intracellular side, EC-to-IC, and from the intracellular side to the extracellular side, IC-to-EC) were recorded separately. We did not record partial (single-plane) crossings. Crossing rates were computed by performing a block average of the accumulated number of permeation events in each direction in blocks of 256 configurations (5.12 ns). The ratio of the EC-to-IC crossing to the IC-to-EC crossing rate was monitored as a function of time until it became stationary around unity, after which we considered the trajectory to be equilibrated. The reported crossing rate values for each simulation system were obtained by linear regression of the accumulated number of permeation events in the EC-to-IC direction as a function of time over the equilibrated portion of each simulation trajectory.

Graph Representations. To characterize connectivity within the permeation pathway of a single AQP0 subunit, we

https://doi.org/10.1021/acs.jpcb.4c03015
J. Phys. Chem. B 2024, 128, 7577−7585

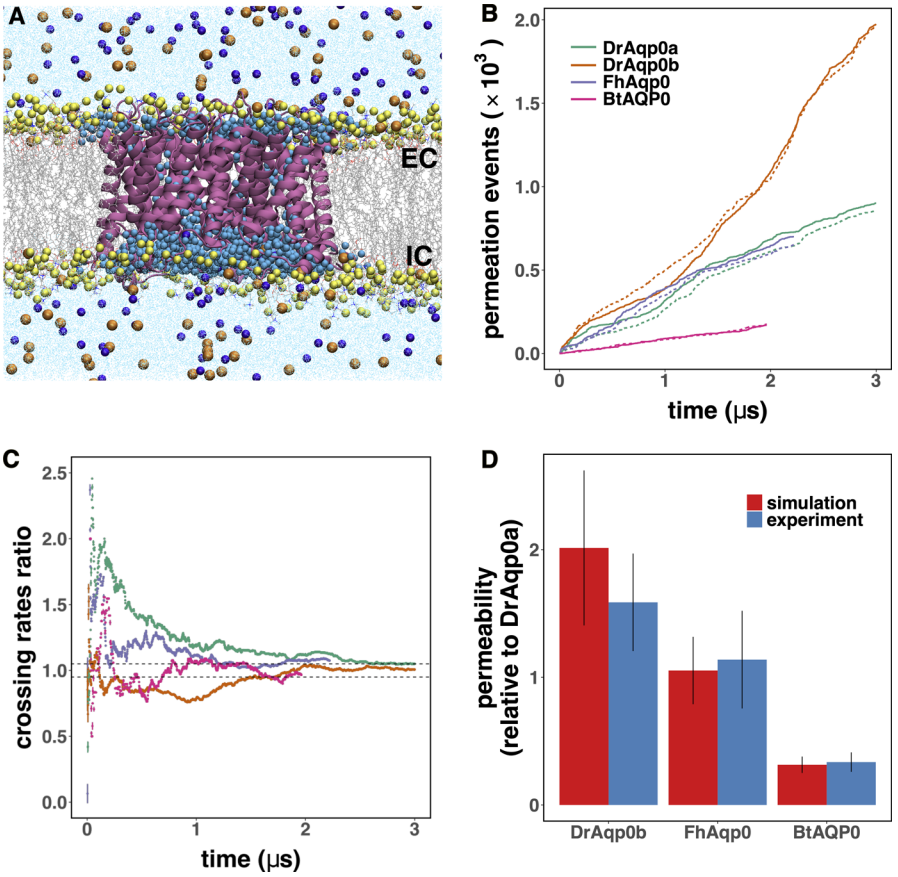

Figure 1. Water permeation through a membrane containing an AQP0 tetramer in the absence of an osmotic gradient. (A) Configuration snapshot showing the AQP0 tetramer in mauve in secondary structure representation. Lipid phosphate P atoms are shown in yellow as filled spheres. Waters within the membrane hydrocarbon core region are shown in cyan as filled spheres. The rest of the waters in the system are shown as cyan dots. Lipid molecules are shown as lines colored by atoms (C, silver; O, red; N, blue; H, white). Na^+ and Cl^- ions are shown in orange and blue filled spheres, respectively. Lipid molecules, ions, and waters outside the membrane hydrocarbon core region are shown in a cut-away view. The membrane surfaces are labeled as extracellular (EC) and intracelullar (IC) according to the orientation of the protein in the plasma membrane. (B) Total number of water permeation events (as defined in the text) as a function of time from the EC side to the IC side (full lines) and from the IC side to the EC side (dashed lines). (C) Ratio of water crossing rates (as defined in the text) as a function of time. Dashed lines corresponding to a crossing rate ratio of 1.05 and 0.95 are shown for reference. (D) Diffusional permeability ratios from simulation compared to corresponding whole-cell osmotic permeability ratios from oocyte swelling assays. The experimental DrAqp0b:DrAqp0a permeability ratio was derived from ref 26, while FhAqp0:DrAqp0a and BtAQP0:DrAqp0a were derived from ref 23. DrAqp0a was chosen as a reference as it was the only AQP0 homolog considered in both experimental reports.

used a graph representation in which the set of vertices consists of water oxygen atoms within a cylindrical region of interest (ROI), heavy atoms from side-chains involved in the AQP0 structural motifs that modulate permeation (R187, H172, F48, F23/Y23, F75, and H66), exposed backbone polar heavy atoms from H61, G64, A65, H66, G180, A181, and G182, and the side-chain nitrogen atoms from N68 and N184. We defined the edges by a distance cutoff of 4 Å or between nonbonded or bonded atoms within a single amino acid side-chain.[45] This set of vertices includes all of the protein heavy atoms in contact with the water single-file. The waters' cylindrical ROI was centered between the nitrogen atoms of N68 and N148 (the Asn residues in the NPA motifs) with 12 Å in radius (spanning the entire channel on the membrane plane) and with a height of 56 Å, which spans the entire protein subunit along the transmembrane direction.

A graph representation was generated for each protein subunit configuration, and all the shortest path connecting waters at both ends of the ROI were determined using bread-first search. We identified these paths as (instantaneous) connected states according to the identity of the connected vertices: "water", for paths involving water oxygen atoms and polar backbone atoms exposed to the conduction pathway; "CS-I", "F/Y23", or "CS-II", if, in addition to water oxygens and backbone polar atoms, the path involves side-chain atoms from residues belonging to those structural motifs. The participation of side-chain atoms from any two or all three structural motifs in the same path were considered as separate connected states. Likewise, if two (or three) separate paths involving different structural motifs were present, we assigned them the corresponding combined connected state. The final connected state assignment for a particular instantaneous configuration of a protein subunit was the one with the least participation of side-chain atoms from any of the three structural motifs. Not all trajectory configurations exhibited a connected path between the ends of the ROI by using this graph representation. Graph representations were generated with a sampling frequency of 20 ps over the entire equilibrated portion of each simulation trajectory. Graph-based analysis and network diagrams were generated with the SNA R package.[46]

https://doi.org/10.1021/acs.jpcb.4c03015
J. Phys. Chem. B 2024, 128, 7577−7585

To estimate transition probability matrices between connected states, we treated the union of sequences of connected states from all four protein subunits over the equilibrated portion of the simulation trajectory as a single discrete time Markov chain from which we calculated the transition matrix using the markovchain R package.[47]

RESULTS AND DISCUSSION

To identify the structural basis underlying the differences in water permeability between zebrafish AQP0 paralogs and between AQP0 mammalian and fish orthologs, we performed equilibrium MD simulations on the microsecond timescale of zebrafish Aqp0a and Aqp0b (DrAqp0a and DrAqp0b), bovine AQP0 (BtAQP0), and AQP0 from killifish (FhAqp0) in a PC:SM:CHL lipid bilayer (see Figure 1A and Table 1).

Table 1. Total and Equilibrated Simulation Trajectory Lengths

simulation system	total trajectory length (μs)	equilibrated trajectory (μs)
DrAqp0a	3.0	1.0
DrAqp0b	3.0	1.0
BtAQP0	2.0	1.2
FhAqp0	2.2	1.0

To account for water permeation through the membrane in the absence of an osmotic gradient, we tracked the position along the transmembrane direction of every water molecule in the system and recorded a permeation event when a water molecule from the bulk solution crosses the headgroup region of one lipid bilayer leaflet into the membrane and exits the membrane region through the opposite membrane surface[48,49] (see Figure 1A,B and Methods section for more details). Under equilibrium conditions, the average number of permeation events per unit time (the crossing rate, q) should be the same in either direction (EC-to-IC and IC-to-EC; see Figure 1A). As shown in Figure 1C, it takes between 1 and 2 μs of simulation trajectory for the corresponding crossing rate ratio to become stationary around unity, which we use here as criterion to determine the equilibrated portion of each trajectory (see Table 1).

The crossing rate, q, over the equilibrated portion of the trajectory can be identified with the membrane's water diffusional permeability coefficient, P_d,[50] by integrating Fick's law along the transmembrane direction via[48−50]

$$q = P_d A c_w \tag{1}$$

where A is the membrane surface area and c_w is the water concentration.

The experimental evidence shows that in pure lipid bilayer membranes, the osmotic water permeability coefficient is $P_f \simeq$

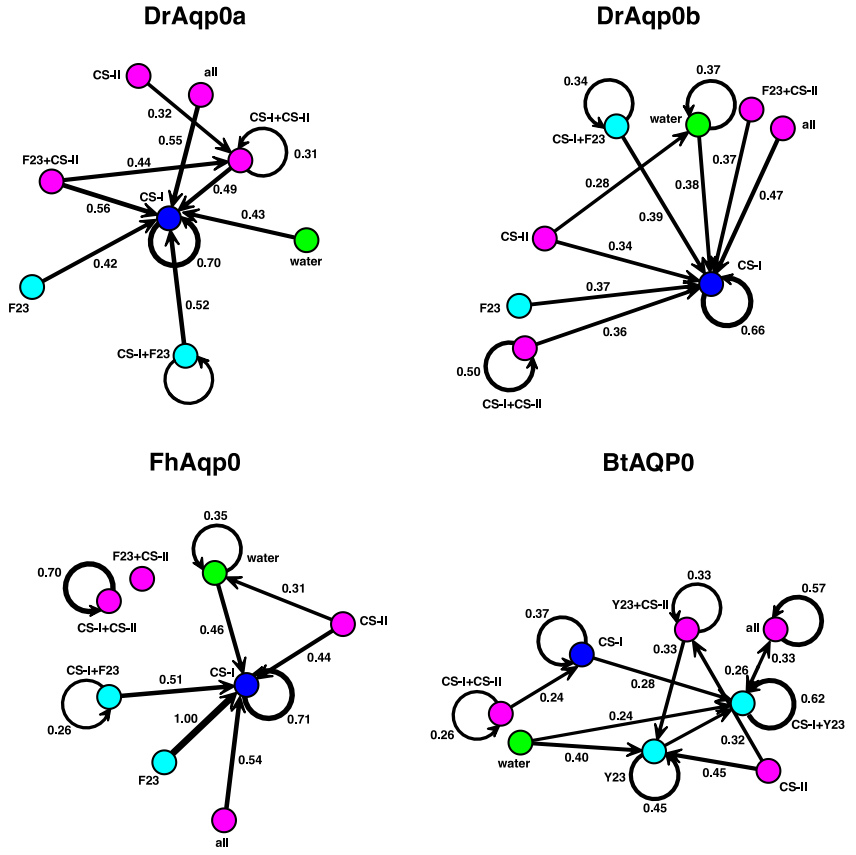

Figure 2. Transition state diagrams summarizing the dynamics of single-file water permeation pathways in each simulation system. In this directed-graph representation, each vertex corresponds to a specific kind connected state (as defined in the text): connected states involving only water molecules and exposed polar backbone atoms are colored green; connected states involving CS-I residue side-chains are colored blue; connected states involving the residue-23 side-chain with or without participation of CS-I are colored cyan; connected states involving CS-II residue side-chains are colored magenta. Only directed-graph edges tying vertices with transition probabilities greater or equal than 0.25 are shown. Edges are labeled with the corresponding transition probability, and their thickness is proportional to the transition probability.

https://doi.org/10.1021/acs.jpcb.4c03015
J. Phys. Chem. B 2024, 128, 7577−7585

P_d.[50] In the case of membrane permeation dominated by single-file diffusion through narrow pores, theory and simulation predict that $P_f/P_d \sim \bar{N}$, with $\bar{N}$ the average number of waters in the channel.[48,51−53] Although the available direct experimental evidence for the P_f/P_d ratio resulting from transport through aquaporins is limited,[54] the results are consistent with the single-file mechanism. Thus, to validate our simulation results using permeability measurements from oocyte swelling assays,[23,26] we make the assumption that different AQP0 homologs will have similar water occupancy implying that under the same experimental conditions, the ratio of their P_f values will be dominated by the specific protein−water interactions of each protein. Such a ratio of two P_f values should be comparable to the corresponding ratio of two P_d values obtained from simulations of the AQP0 homolog embedded in the same lipid bilayer system and performed under the same conditions. We find under this assumption, that our simulations reproduce the experimental trends,[23,26] as shown in Figure 1D.

Protein−water interactions modulate water transport though AQP channels.[19] We have previously derived mechanistic insights into AQP0 osmotic transport by characterizing the dynamics of the network formed by waters and amino acid residues exposed to the permeation pathway.[45] Here, we follow a similar approach with our equilibrium simulations. In particular, for each simulation configuration, we generate an instantaneous graph representation of each AQP0 subunit (as described in detail in the Methods section) and determine the shortest path across the channel pathway connecting waters at both ends of the protein subunit that most resembles an uninterrupted water single-file. We classify these "connected states" according to the identity of the graph vertices forming the path as "water" involving only water molecules and backbone polar atoms exposed to the pathway: "Y23/F23", involving waters, exposed backbone polar atoms, and the residue-23 side-chain; "CS-I" or "CS-II", involving waters, exposed backbone polar atoms, and residue side-chain atoms from either CS-I or CS-II. We also consider compound connected states involving atoms from CS-I, CS-II, and/or residue-23. We used the combined results from all four protein subunits to estimate transition probabilities between connected states. The corresponding transition state diagrams for each simulation system are shown in Figure 2, where only transition probabilities greater than or equal to 0.25 are shown for clarity. The corresponding overall distribution of connected states per simulation system over the equilibrated portion of the simulation trajectory is shown in Figure 3.

As shown in Figure 2, configurations involving the participation of Y23 in the single file configuration dominate the dynamics in bovine AQP0 with a transition to a pathway closed at CS-I being the most likely (Figure 3). The prevalence of a pathway closed at CS-II also appears to be subordinated to the participation of Y23 in the single file configuration (Figure 2). Similarly, there are not likely transitions to an uninterrupted water single-file from a closed state. The central role in water permeation through bovine AQP0 exhibited by Y23 is consistent with previous simulation studies[27,45,55−57] and limited experimental evidence from AQP0 in proteoliposomes showing a roughly a 10-fold increase in water permeability upon Y23F substitution in AQP0 from sheep.[27] A configuration of the single-file pathway involving Y23 that is closed at both CS-I and CS-II is also very likely in bovine

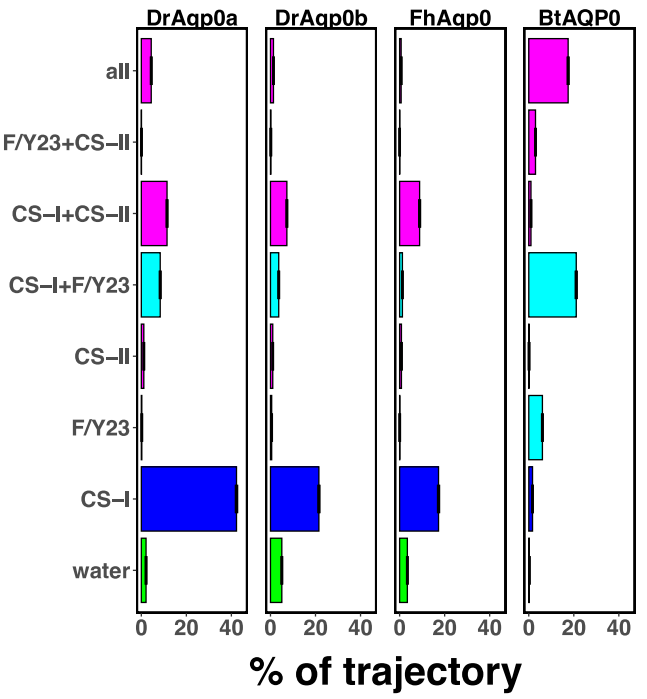

Figure 3. Overall distribution of connected states as a percentage of trajectory configurations. Error bars are proportion standard error estimates. The color scheme is the same as in Figure 2.

AQP0 (Figure 3) resulting from transitions between open and closed configurations at CS-II (Figure 3), which is consistent with the role of CS-II as a channel gate that has emerged from both experiments and simulations.[5,27,45,57]

In contrast to bovine AQP0, in all three fish AQP0 systems, the most likely transition from an arbitrary connected state is to a configuration where the pore is closed at CS-I (Figure 2). Connected states that include F23 in the single file configuration are always accompanied by CS-I, and their frequency is correlated to that of "CS-I only" connected states across all three fish AQP0 (Figure 3). Thus, without the hydroxyl moiety, the engagement of residue-23 with the water single-file appears to be likely part of the CS-I closed state dynamics, suggesting that overall permeation is mainly regulated by the opening and closing of CS-I, which is the canonical mechanism for water selective aquaporins.[19,20]

The most salient difference emerging from this analysis comparing zebrafish Aqp0a and Aqp0b is the appearance of a significant population of open configurations in Aqp0b (Figure 3) arising from an increase in the transition probability between open connected states and from a CS-II connected state to an open state (Figure 2). A similar increase in the frequency of open states and corresponding increase in transition probabilities are also observed in killifish AQP0. However, in contrast to Aqp0b, transitions from a connected state closed at CS-II to a connected state closed only at CS-I are less likely in killifish AQP0 (Figure 2). These changes in open channel probability and participation of CS-II in the single file configuration are consistent with both the water permeability increase in zebrafish Aqp0b relative to Aqp0a and the similar water permeabilities for both zebrafish Aqp0a and killifish AQP0 (Figure 1D).

In mammalian AQP0, both CS-I and Y23 appear to have well delineated roles in the modulation of water permeation with Y23 acting as a "static" gate moderating water flow, in

https://doi.org/10.1021/acs.jpcb.4c03015
J. Phys. Chem. B 2024, 128, 7577−7585

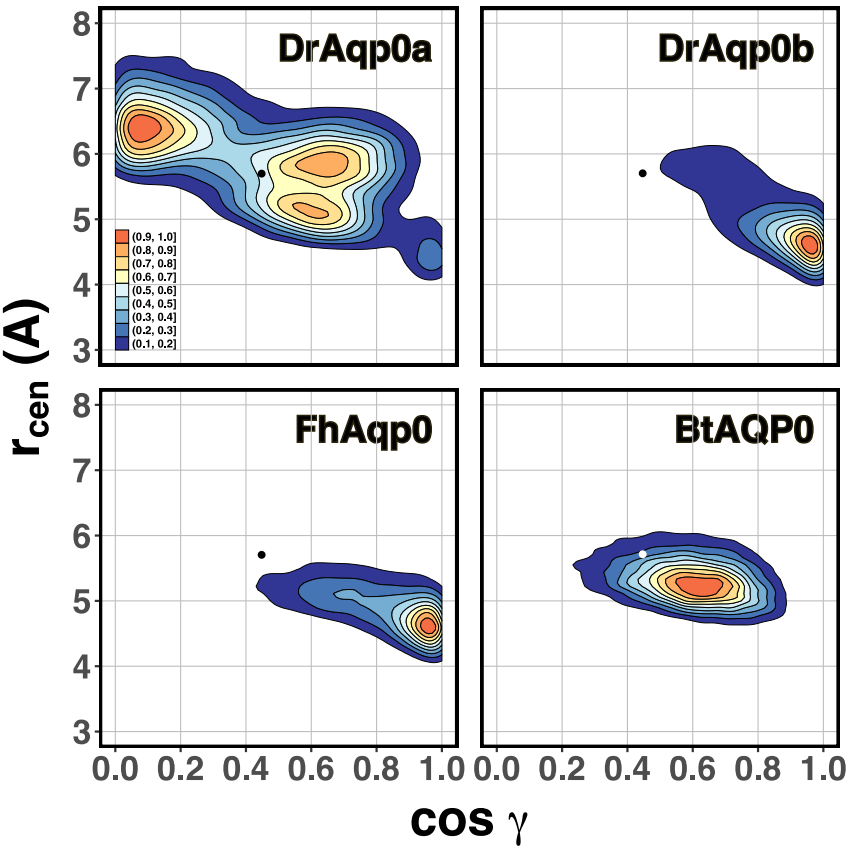

Figure 4. Spatial configuration of the F23−F48 (fish) and Y23−F48 (bovine) side-chain pairs shown as joint kernel density estimates of the angle between the rings' normal vectors (γ) and the distance between the rings' geometric centers (r_{cen}). The filled contours are scaled densities. The corresponding configuration in the bovine AQP0 crystallographic structure,[21] which is also the same configuration in all three fish AQP0 AlphaFold structures, is highlighted as dots

which the configurational dynamics of R187 in CS-I regulates the access of waters from the EC vestibule into the single-file pathway.[22] The prevalence of a closed/blocked configuration involving both CS-I and Y23 mediated by a water H bond would account for the notably low permeability of mammalian AQP0.[27,45] If the substitution of Y23 by F23 in fish aquaporins abolishes this putative most favored configuration, what are the consequences to overall dynamics of CS-I? In particular, the proximity of residue-23 and F48 in CS-I suggests the possibility of $\pi-\pi$ stacking interactions between both phenylalanine side-chains. As shown in Figure 4, the configurational landscape of the F23−F48 (fish) and Y23−F48 (mammalian) side-chain pairs shows rather narrow joint distributions for the distance between ring centroids and their relative orientation in all systems except for zebrafish Aqp0a. The corresponding configuration in the bovine AQP0 crystallographic structure,[21] which is also the same configuration in all three fish AQP0 AlphaFold structures, is highlighted as a dot in Figure 4.The fact that these 2-D densities are generated from all four protein subunits suggests a preference for specific orientations of the two side-chains. In bovine AQP0, the relative orientation of the Y23−F48 side-chains remains similar to the crystallographic structure and does not suggest a stacking interaction and appears to be consistent with an interaction mediated by the water single-file, as described above. In contrast, the dominant relative orientation and separation of the F23−F48 side-chains in zebrafish Aqp0a and FhAqp0 is one consistent with a parallel $\pi-\pi$ stacking interaction (Figure 4). Zebrafish Aqp0a does not show a preferred configuration; the most likely arrangement suggests little or no association between the F23 and F48 side-chains (Figure 4). The results show no significant association between the initial configuration of the F23−F48 side-chains and the sampled landscape over the equilibrated portion of the fish AQP0 simulation trajectories, which indicates that the differences in conformational dynamics across systems are independent of the AlphaFold structure predictions.

What are the consequences of a preferred configuration between F23 and F48 for water permeation? In zebrafish Aqp0b and killifish AQP0, the substitution of Y23 for F23 not only abolishes the key structural feature of single-file transport in mamallian AQP0 but also affects the conformational dynamics of CS-I. The role of CS-I as structural constriction relies on the interactions between the phenyl and imidazole moieties from F48 and H172, respectively, with the guanidium moiety in the more flexible R187 side-chain. A persistent direct interaction between F48 and F23 would result in less engagement between F48 and R187. We evaluated the configurational landscape of the F48 phenyl and R187 gaunidinium moiety pair in the same manner as for the F23−F48 phenyl pair; the corresponding 2-D density estimates, as well as the configuration in the crystallographic structure, are shown in (Figure 5). A parallel or close to parallel arrangement is now prevalent in bovine and zebrafish Aqp0a, which is consistent with the prevalence of the CS-I + Y23 and CS-I connected states, respectively (Figure 3). At the opposite end, zebrafish Aqp0b exhibits only minor engagement between R187 and F48 consistent with the notion of CS-I

https://doi.org/10.1021/acs.jpcb.4c03015
J. Phys. Chem. B 2024, 128, 7577−7585

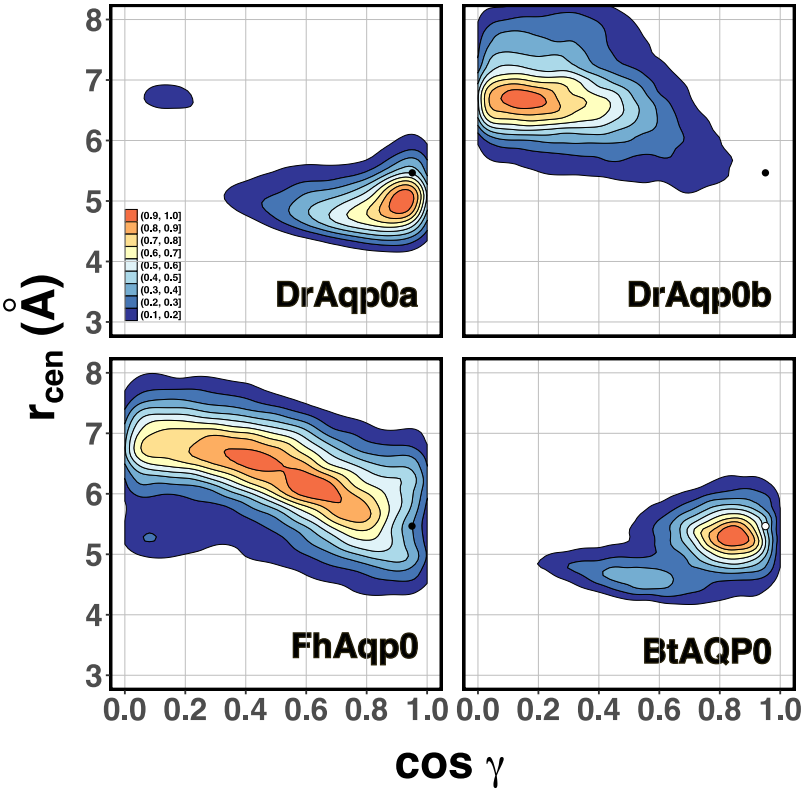

Figure 5. Spatial configuration of the F48−R187 phenyl−guanidinium groups shown as joint kernel density estimates of the angle between the phenyl and guanidinium moieties normal vectors (γ) and the distance between the phenyl and guanidinium moieties centers of mass (r_{cen}). The filled contours are scaled densities. The corresponding configuration in the bovine AQP0 crystallographic structure,[21] which is also the same configuration in all three fish AQP0 AlphaFold structures, is highlighted as dots.

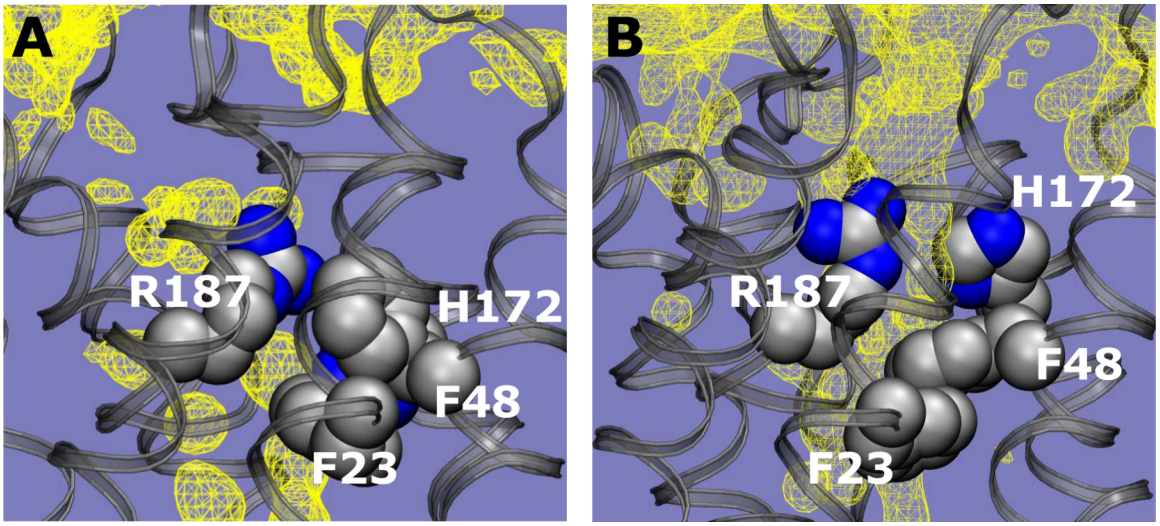

Figure 6. Configuration snapshots of the EC vestibule in a subunit of (A) zebrafish Aqp0a in a closed CS-I configuration and (B) zebrafish Aqp0b in an open CS-I configuration. The CS-I side-chains and F23 heavy atoms are shown as filled spheres colored by atoms (C, silver; N, blue). The protein is shown in secondary structure representation. Water distributions are shown as a surface of equal occupancy at 25%. Increased open CS-I configurations in zebrafish Aqp0b are consistent with an increased water occupancy in the EC vestibule relative to Aqp0a. The closed CS-I configuration of Aqp0a shows tight packing of the CS-I side-chains with limited interaction between F48 and F23. In contrast, the open configuration of CS-I shows parallel stacking of F48 and F23.

open configurations being more likely in Aqp0b than in Aqp0a (Figure 3). Killifish AQP0 shows no preferential configuration for the R187−F48 pair, but the overall distribution could be considered to be between those of zebrafish Aqp0b and Aqp0a, suggesting that the presence of F23 allows for a significant population of configurations with CS-I open when F48 engages with F23 and CS-I closed configurations when F48 remains engaged with R187.

Taken together, our simulation results provide some underlying structural insights that could explain the difference

https://doi.org/10.1021/acs.jpcb.4c03015
J. Phys. Chem. B 2024, 128, 7577−7585

in water permeability between zebrafish Aqp0a and Aqp0b. However, for the alternate engagement mechanism of F48 between CS-I and F23 to translate into an increase in the CS-I open probability, it would be necessary to account for the solvation of the R187 guanidinium moiety in the open configuration of CS-I. As shown in Figure 6, the EC vestibule in zebrafish Aqp0b appears significantly more hydrated than in Aqp0a, and this is consistent with the notion of an increase in the open probability of CS-I that would translate in an increase in water permeability.

CONCLUSIONS

The presence of Y23 in the mammalian AQP0 water permeation pathway is a distinctive structural feature that has been suggested to account for the notably low AQP0 permeability. Our fish AQP0 simulations on the microsecond timescale reveal that the substitution of Y23 by F23 in fish orthologs goes beyond the simple removal of a barrier to the water single-file by inducing a richer conformational landscape of the CS-I structural motif that may account for the difference in water permeability between mammalian and fish AQP0 orthologs and between the zebrafish AQP0 paralogs.

AUTHOR INFORMATION

Corresponding Author

Douglas J. Tobias − *Department of Chemistry, University of California, Irvine, Irvine, California 92697-2025, United States;* orcid.org/0000-0002-6971-9828; Email: dtobias@uci.edu

Author

J. Alfredo Freites − *Department of Chemistry, University of California, Irvine, Irvine, California 92697-2025, United States;* orcid.org/0000-0001-5842-7443

Complete contact information is available at: https://pubs.acs.org/10.1021/acs.jpcb.4c03015

Notes

The authors declare no competing financial interest.

ACKNOWLEDGMENTS

The authors thank Drs. James Hall, Tom Schilling, Olga Safrina, Paul Donaldson, and Irene Vorontosova for helpful discussions. This work was supported by the National Institutes of Health (Grant R01EY031587 to D.J.T.). The computations were carried on the Greenplanet high-performance computing cluster operated by the School of Physical Sciences at UC Irvine. We are grateful to Dr. Nathan Crawford for outstanding technical support.

REFERENCES

(1) Donaldson, P. J.; Grey, A. C.; Maceo Heilman, B.; Lim, J. C.; Vaghefi, E. The physiological optics of the lens. *Prog. Retin Eye Res.* **2017**, *56*, e1−e24.

(2) Schey, K. L.; Gletten, R. B.; O'Neale, C. V. T.; Wang, Z.; Petrova, R. S.; Donaldson, P. J. Lens Aquaporins in Health and Disease: Location is Everything. *Front Physiol* **2022**, *13*, 882550.

(3) Chandy, G.; Zampighi, G. A.; Kreman, M.; Hall, J. E. Comparison of the water transporting properties of MIP and AQP1. *J. Membr. Biol.* **1997**, *159*, 29−39.

(4) Mulders, S. M.; Preston, G. M.; Deen, P. M.; Guggino, W. B.; van Os, C. H.; Agre, P. Water channel properties of major intrinsic protein of lens. *J. Biol. Chem.* **1995**, *270*, 9010−16.

(5) Clemens, D. M.; Németh-Cahalan, K. L.; Trinh, L.; Zhang, T.; Schilling, T. F.; Hall, J. E. In vivo analysis of aquaporin 0 function in zebrafish: permeability regulation is required for lens transparency. *Invest Ophthalmol Vis Sci.* **2013**, *54*, 5136−43.

(6) Vorontsova, I.; Vallmitjana, A.; Torrado, B.; Schilling, T. F.; Hall, J. E.; Gratton, E.; Malacrida, L. In vivo macromolecular crowding is differentially modulated by aquaporin 0 in zebrafish lens: Insights from a nanoenvironment sensor and spectral imaging. *Sci. Adv.* **2022**, *8*, No. eabj4833.

(7) Zampighi, G. A.; Simon, S. A.; Hall, J. E. The specialized junctions of the lens. *Int. Rev. Cytol* **1992**, *136*, 185−225.

(8) Gonen, T.; Cheng, Y.; Sliz, P.; Hiroaki, Y.; Fujiyoshi, Y.; Harrison, S. C.; Walz, T. Lipid−protein interactions in double-layered two-dimensional AQP0 crystals. *Nature* **2005**, *438*, 633−638.

(9) Gonen, T.; Sliz, P.; Kistler, J.; Cheng, Y.; Walz, T. Aquaporin-0 membrane junctions reveal the structure of a closed water pore. *Nature* **2004**, *429*, 193−7.

(10) Kumari, S. S.; Varadaraj, K. Intact AQP0 performs cell-to-cell adhesion. *Biochem. Biophys. Res. Commun.* **2009**, *390*, 1034−9.

(11) Vorontsova, I.; Gehring, I.; Hall, J. E.; Schilling, T. F. Aqp0a Regulates Suture Stability in the Zebrafish Lens. *Invest Ophthalmol Vis Sci.* **2018**, *59*, 2869−2879.

(12) Lindsey Rose, K. M.; Gourdie, R. G.; Prescott, A. R.; Quinlan, R. A.; Crouch, R. K.; Schey, K. L. The C terminus of lens aquaporin 0 interacts with the cytoskeletal proteins filensin and CP49. *Invest Ophthalmol Vis Sci.* **2006**, *47*, 1562−70.

(13) Wang, Z.; Schey, K. L. Aquaporin-0 interacts with the FERM domain of ezrin/radixin/moesin proteins in the ocular lens. *Invest Ophthalmol Vis Sci.* **2011**, *52*, 5079−87.

(14) Nakazawa, Y.; Oka, M.; Mitsuishi, A.; Bando, M.; Takehana, M. The effect of the interaction between aquaporin 0 (AQP0) and the filensin tail region on AQP0 water permeability. *Mol. Vis* **2011**, *17*, 3191−9.

(15) Shiels, A.; Bennett, T. M.; Hejtmancik, J. F. Cat-Map: putting cataract on the map. *Mol. Vis* **2010**, *16*, 2007−15.

(16) Qin, L.; Guo, L.; Wang, H.; Li, T.; Lou, G.; Guo, Q.; Hou, Q.; Liu, H.; Liao, S.; Liu, Z. A novel MIP mutation in familial congenital nuclear cataracts. *Eur. J. Med. Genet* **2016**, *59*, 488−91.

(17) Liu, S.; Zhu, P.; Ni, M.; Zhang, M.; Jiang, W.; Yu, M.; Zhang, J.; Wu, Q.; Li, W.; Xue, C.; et al. A novel mutation of MIP in a Chinese family with congenital nuclear cataract identified by whole-exome sequencing. *Ophthalmic Genet* **2018**, *39*, 139−140.

(18) Zeidel, M. L.; Ambudkar, S. V.; Smith, B. L.; Agre, P. Reconstitution of functional water channels in liposomes containing purified red cell CHIP28 protein. *Biochemistry* **1992**, *31*, 7436−40.

(19) Murata, K.; Mitsuoka, K.; Hirai, T.; Walz, T.; Agre, P.; Heymann, J. B.; Engel, A.; Fujiyoshi, Y. Structural determinants of water permeation through aquaporin-1. *Nature* **2000**, *407*, 599−605.

(20) de Groot, B. L.; Grubmüller, H. The dynamics and energetics of water permeation and proton exclusion in aquaporins. *Curr. Opin. Struct. Biol.* **2005**, *15*, 176−183.

(21) Harries, W. E.; Akhavan, D.; Miercke, L. J.; Khademi, S.; Stroud, R. M. The channel architecture of aquaporin 0 at a 2.2-Å resolution. *Proc. Natl. Acad. Sci. U. S. A.* **2004**, *101*, 14045−14050.

(22) Hall, J. E.; Freites, J. A.; Tobias, D. J. Experimental and Simulation Studies of Aquaporin 0 Water Permeability and Regulation. *Chem. Rev.* **2019**, *119*, 6015−6039.

(23) Froger, A.; Clemens, D.; Kalman, K.; Németh-Cahalan, K. L.; Schilling, T. F.; Hall, J. E. Two distinct aquaporin 0s required for development and transparency of the zebrafish lens. *Invest Ophthalmol Vis Sci.* **2010**, *51*, 6582−92.

(24) Wang, K.; Vorontsova, I.; Hoshino, M.; Uesugi, K.; Yagi, N.; Hall, J. E.; Schilling, T. F.; Pierscionek, B. K. Aquaporins Have Regional Functions in Development of Refractive Index in the Zebrafish Eye Lens. *Invest Ophthalmol Vis Sci.* **2021**, *62*, 23.

(25) Tingaud-Sequeira, A.; Calusinska, M.; Finn, R. N.; Chauvigné, F.; Lozano, J.; Cerdà, J. The zebrafish genome encodes the largest vertebrate repertoire of functional aquaporins with dual paralogy and

substrate specificities similar to mammals. *BMC Evol Biol.* **2010**, *10*, 38.
(26) Chauvigné, F.; Zapater, C.; Stavang, J. A.; Taranger, G. L.; Cerdà, J.; Finn, R. N. The pH sensitivity of Aqp0 channels in tetraploid and diploid teleosts. *FASEB J.* **2015**, *29*, 2172−2184.
(27) Saboe, P. O.; Rapisarda, C.; Kaptan, S.; Hsiao, Y.-S.; Summers, S. R.; De Zorzi, R.; Dukovski, D.; Yu, J.; De Groot, B. L.; Kumar, M.; et al. Role of pore-lining residues in defining the rate of water conduction by aquaporin-0. *Biophys. J.* **2017**, *112*, 953−965.
(28) Jumper, J.; Evans, R.; Pritzel, A.; Green, T.; Figurnov, M.; Ronneberger, O.; Tunyasuvunakool, K.; Bates, R.; Žídek, A.; Potapenko, A.; et al. Highly accurate protein structure prediction with AlphaFold. *Nature* **2021**, *596*, 583−589.
(29) Varadi, M.; Anyango, S.; Deshpande, M.; Nair, S.; Natassia, C.; Yordanova, G.; Yuan, D.; Stroe, O.; Wood, G.; Laydon, A.; et al. AlphaFold Protein Structure Database: massively expanding the structural coverage of protein-sequence space with high-accuracy models. *Nucleic Acids Res.* **2022**, *50*, D439−D444.
(30) Jo, S.; Lim, J. B.; Klauda, J. B.; Im, W. CHARMM-GUI Membrane Builder for mixed bilayers and its application to yeast membranes. *Biophys. J.* **2009**, *97*, 50−58.
(31) Wu, E. L.; Cheng, X.; Jo, S.; Rui, H.; Song, K. C.; Dávila-Contreras, E. M.; Qi, Y.; Lee, J.; Monje-Galvan, V.; Venable, R. M.; et al. CHARMM-GUI Membrane Builder toward realistic biological membrane simulations. *J. Comput. Chem.* **2014**, *35*, 1997−2004.
(32) Humphrey, W.; Dalke, A.; Schulten, K. VMD: Visual molecular dynamics. *J. Mol. Graph.* **1996**, *14*, 33−38.
(33) Lomize, M. A.; Pogozheva, I. D.; Joo, H.; Mosberg, H. I.; Lomize, A. L. OPM database and PPM web server: resources for positioning of proteins in membranes. *Nucleic Acids Res.* **2012**, *40*, D370−D376.
(34) Phillips, J. C.; Hardy, D. J.; Maia, J. D. C.; Stone, J. E.; Ribeiro, J. V.; Bernardi, R. C.; Buch, R.; Fiorin, G.; Hénin, J.; Jiang, W.; et al. Scalable molecular dynamics on CPU and GPU architectures with NAMD. *J. Chem. Phys.* **2020**, *153*, 044130.
(35) Huang, J.; Rauscher, S.; Nawrocki, G.; Ran, T.; Feig, M.; de Groot, B. L.; Grubmüller, H.; MacKerell, A. D. CHARMM36m: an improved force field for folded and intrinsically disordered proteins. *Nat. Methods* **2017**, *14*, 71−73.
(36) Klauda, J. B.; Venable, R. M.; Freites, J. A.; O'Connor, J. W.; Tobias, D. J.; Mondragon-Ramirez, C.; Vorobyov, I.; MacKerell Jr, A. D.; Pastor, R. W. Update of the CHARMM all-atom additive force field for lipids: validation on six lipid types. *J. Phys. Chem. B* **2010**, *114*, 7830−7843.
(37) Jorgensen, W.; Chandrasekhar, J.; Madura, J.; Impey, R.; Klein, M. Comparison of simple potential functions for simulating liquid water. *J. Chem. Phys.* **1983**, *79*, 926−935.
(38) Darden, T.; York, D.; Pedersen, L. Particle mesh Ewald: An N log(N) method for Ewald sums in large systems. *J. Chem. Phys.* **1993**, *98*, 10089−10092.
(39) Essmann, U.; Perera, L.; Berkowitz, M. L.; Darden, T.; Lee, H.; Pedersen, L. G. A smooth particle mesh Ewald method. *J. Chem. Phys.* **1995**, *103*, 8577−8593.
(40) Grubmüller, H.; Heller, H.; Windemuth, A.; Schulten, K. Generalized Verlet Algorithm for Efficient Molecular Dynamics Simulations with Long-range Interactions. *Mol. Sim.* **1991**, *6*, 121−142.
(41) Ryckaert, J.-P.; Ciccotti, G.; Berendsen, H. Numerical integration of the Cartesian equations of motion of a system with constraints: Molecular dynamics of n-alkanes. *J. Comput. Phys.* **1977**, *23*, 327−341.
(42) Martyna, G.; Tobias, D.; Klein, M. Constant-pressure molecular-dynamics algorithms. *J. Chem. Phys.* **1994**, *101*, 4177−4189.
(43) Feller, S. E.; Zhang, Y.; Pastor, R. W.; Brooks, B. R. Constant pressure molecular dynamics simulation: The Langevin piston method. *J. Chem. Phys.* **1995**, *103*, 4613−4621.
(44) R Core Team R: *A Language and Environment for Statistical Computing*; R Foundation for Statistical Computing: Vienna, Austria, 2016.
(45) Freites, J. A.; Németh-Cahalan, K. L.; Hall, J. E.; Tobias, D. J. Cooperativity and allostery in aquaporin 0 regulation by Ca2. *Biochim Biophys Acta Biomembr* **2019**, *1861*, 988−996.
(46) Butts, C. Social Network Analysis with sna. *J. Stat. Softw.* **2008**, *24*, 1−51.
(47) Spedicato, G. A. Discrete Time Markov Chains with R. *R Journal* **2017**, *9*, 84−104.
(48) Zhu, F.; Tajkhorshid, E.; Schulten, K. Pressure-induced water transport in membrane channels studied by molecular dynamics. *Biophys. J.* **2002**, *83*, 154−60.
(49) Venable, R. M.; Krämer, A.; Pastor, R. W. Molecular Dynamics Simulations of Membrane Permeability. *Chem. Rev.* **2019**, *119*, 5954−5997.
(50) Cass, A.; Finkelstein, A. Water permeability of thin lipid membranes. *J. Gen Physiol* **1967**, *50*, 1765−84.
(51) Levitt, D. G. A new theory of transport for cell membrane pores. I. General theory and application to red cell. *Biochim. Biophys. Acta* **1974**, *373*, 115−31.
(52) Berezhkovskii, A.; Hummer, G. Single-file transport of water molecules through a carbon nanotube. *Phys. Rev. Lett.* **2002**, *89*, 064503.
(53) de Groot, B. L.; Tieleman, D. P.; Pohl, P.; Grubmüller, H. Water permeation through gramicidin A: desformylation and the double helix: a molecular dynamics study. *Biophys. J.* **2002**, *82*, 2934−42.
(54) Mathai, J. C.; Mori, S.; Smith, B. L.; Preston, G. M.; Mohandas, N.; Collins, M.; van Zijl, P. C.; Zeidel, M. L.; Agre, P. Functional analysis of aquaporin-1 deficient red cells. The Colton-null phenotype. *J. Biol. Chem.* **1996**, *271*, 1309−13.
(55) Hashido, M.; Ikeguchi, M.; Kidera, A. Comparative simulations of aquaporin family: AQP1, AQPZ, AQP0 and GlpF. *FEBS Lett.* **2005**, *579*, 5549−52.
(56) Han, B.-G.; Guliaev, A. B.; Walian, P. J.; Jap, B. K. Water transport in AQP0 aquaporin: molecular dynamics studies. *J. Mol. Biol.* **2006**, *360*, 285−96.
(57) Jensen, M. Ø.; Dror, R. O.; Xu, H.; Borhani, D. W.; Arkin, I. T.; Eastwood, M. P.; Shaw, D. E. Dynamic control of slow water transport by aquaporin 0: implications for hydration and junction stability in the eye lens. *Proc. Natl. Acad. Sci. U. S. A.* **2008**, *105*, 14430−14435.

https://doi.org/10.1021/acs.jpcb.4c03015
J. Phys. Chem. B 2024, 128, 7577−7585